Identifying Problematic Phase Transformations in Pb Foil Anodes for Sodium-Ion Batteries

To cite this article: Jia Zhang *et al* 2024 *J. Electrochem. Soc.* **171** 090516
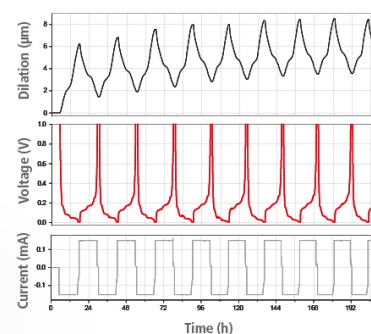
View the article online for updates and enhancements.

Identifying Problematic Phase Transformations in Pb Foil Anodes for Sodium-Ion Batteries

Jia Zhang,[1] Tianye Zheng,[1,2,z] Xiaoyang Guo,[3] Hung Quoc Nguyen,[4] Ka-wai Eric Cheng,[1] Kwok-Ho Lam,[1,5] Daniel Rettenwander,[4] Wei Jin,[1,2] and Steven T. Boles[3,6,*]

[1]*Department of Electrical and Electronic Engineering, The Hong Kong Polytechnic University, Hung Hom, Kowloon, Hong Kong*
[2]*Photonics Research Institute, The Hong Kong Polytechnic University, Hung Hom, Kowloon, Hong Kong*
[3]*Department of Energy and Process Engineering, Faculty of Engineering, Norwegian University of Science and Technology (NTNU), Trondheim, Norway*
[4]*Department of Material Science and Engineering, Faculty of Natural Science, Norwegian University of Science and Technology (NTNU), Trondheim, Norway*
[5]*Centre for Medical and Industrial Ultrasonics, James Watt School of Engineering, University of Glasgow, Glasgow, Scotland, United Kingdom*
[6]*Centre for Advances in Reliability and Safety (CAiRS), Hong Kong Science Park, New Territories, Hong Kong*

Group IVA elements have aroused attention in sodium-ion batteries (SIBs) due to their Na-storage capability. Among them, Pb is less explored perhaps due to its perceived risks, but its long-standing success in Pb-acid batteries should not be neglected. Together with the well-established recycling procedures, the merits of Pb warrant further investigations as a practical SIB anode. In this work, four intermetallic phases are detected during electrochemical sodiation of Pb, which yields a capacity of $\sim$460 mAh·g^{-1} ($\sim$1167 mAh·cm^{-3}) upon the formation of Na$_{15}$Pb$_4$. When pursuing full capacities, the electrode stops functioning after only 3–4 cycles largely due to electrode physical damage. The reversibility of each phase transformation pair is then assessed to explore the origins of capacity fading. The NaPb/Na$_9$Pb$_4$ transformation shows the worst stability, consistent with the observed structural damage (e.g., cracks and voids). Through bypassing the problematic phase transformations using a partial cycling protocol, the stability of Pb foil anodes is improved, giving 20 cycles with 85% capacity retention. Considering other factors are unoptimized, it is suggested that the Pb-based anodes should not be fully eliminated from the future roadmap of SIBs, as the prospective merits can create value to ensure the management of such materials of concern.

Supplementary material for this article is available online

Thanks to the similar chemistry to lithium-ion batteries (LIBs), sodium-ion batteries (SIBs) are considered a sustainable and cost-effective alternative to LIBs, particularly in emerging large-scale energy storage applications due to the abundance and uniform geographic distribution of Na on Earth.[1] Over the past decade, SIBs have been experiencing rapid developments because of the knowledge and strategies accumulated in analogous LIBs.[2] Simply adopting LIB electrodes to the SIB system may be the easiest approach but is not always successful due to the anomalies between the two systems, such as the ionic radius of Na$^+$, chemical bonds associated with Na, and thermodynamics of Na-based systems.[3] While heavier and larger Na$^+$ (0.102 nm vs 0.076 nm for Li$^+$) would be expected to migrate relatively slowly in electrode materials, increasing electrochemical polarization, structural considerations in the host materials are also known to play a key role in governing transport characteristics.[4] Concerning anode host materials, a larger volume is required for accommodating the incorporation of Na$^+$ (as compared to Li$^+$), as a result, it is more challenging to find stable anode candidates for SIBs that display competitive cycling stability.[5] Graphitic carbon, the most successfully commercialized anode in LIBs, exhibits very limited Na storage capability because the formation of stable Na-intercalated graphite compounds is thermodynamically unfavorable due to the weak bonding force between C and Na.[3,6] On the contrary, hard carbon (HC), with a lower degree of graphitization compared to graphite,[7] is widely considered to be the most promising electrode candidate for SIBs, given its advantages of moderate capacity (ca. 350 mAh·g^{-1}), low cost, sustainability, and environmental footprint. However, its low initial coulombic efficiency (ICE) remains an issue because Na ions can be irreversibly inserted into the defect sites of

HC, yielding a reversible capacity of only ca. 150 mAh·g^{-1}.[8] The cycle life of HC, normally 200–300 cycles,[9] is also not satisfactory for sustainability-minded applications. From a safety dimension, Na deposition poses a continued risk, as it can hardly be prevented due to the low sodiation potential of HC, especially under fast charging conditions and/or low temperatures. In industry, the production of HC often requires high-temperature carbonization in an inert atmosphere, which is complicated and energy-consuming,[10] although it does present a bio-sourcing pathway seldom seen in the battery sector.

In addition to the carbon-based materials, some alloy anode candidates also exhibit interesting Na storage capabilities. Among them, Si is found to be electrochemically inactive to Na, even at elevated temperatures up to 80 °C, regardless of crystalline or amorphous states.[11] While no solid conclusion can be drawn, the unfavorable electrochemical sodiation of Si is suggested to be associated with sluggish Na diffusion in the Na-Si matrix, weak bonding between Na and Si, and poor electrical conductivity of Si.[11] Ge, sharing the same crystal structure as that of Si but with a slightly larger lattice constant, can only be electrochemically sodiated in its amorphous state at room temperature, giving a reversible capacity of $\sim$300 mAh·g^{-1}.[11] Sn, Sb, P, and Bi also have shown some Na-storage capabilities: Experimentally, they exhibit initial capacities of 856–878 mAh·g^{-1},[12–14] 540–600 mAh·g^{-1},[15] 600–1814 mAh·g^{-1},[16] and 400 mAh·g^{-1},[17] respectively. Therefore, numerous studies have focused on these alloy electrodes, and the past decade witnessed significant advances in their electrochemical storage performances.[18–20] However, they all suffer from poor cycling performances caused by mechanical failures, such as cracking and pulverization.[10] Like the situation of LIBs, alloy-type anodes for SIBs have long-standing challenges, especially when application standards are considered. Therefore, further understanding of new electrode candidates and the governing factors leading to reasonable capacity, satisfactory cycle life, and enhanced safety is warranted in the SIB field.

*Electrochemical Society Member.
[z]E-mail: darren.ty.zheng@connect.polyu.hk

Amongst the alloy anode candidates for SIBs, Pb is known to form a highly-sodiated phase of $Na_{15}Pb_4$, yielding a specific capacity of 485 mAh·g^{-1} or 1175 mAh·cm^{-3} (with respect to the volume of $Na_{15}Pb_4$ alloy).[21,22] However, Pb or Pb-based materials, which are often neglected by the community due to their toxicity and environmental concerns, have been subject to notable industrial restrictions in the past, such as RoHS and REACH. With such scrutiny, it is only natural that supply chain tightening has coincided with a recycling rate of Pb that is currently more than 99%, marking one of the highest material recycling rates worldwide.[23] As noted in a recently published paper,[24] all Pb-containing components are reported to be readily recycled from Pb-acid batteries (PABs). For SIBs, besides the attractive volumetric capacity, the Pb electrode also possesses the metrics of cost-effectiveness (around \$2 per kg),[25] high abundance, and acceptable electric conductivity.[21,22] In addition, the large atomic size of Pb can offer more interstitial space to accommodate Na, likely resulting in more favorable sodiation kinetics.[22] Still, common to all alloy anodes, Pb also suffers from the structural failure induced by volume changes upon (de-)sodiation, and therefore a poor cycle life.[26] For example, an early study showed that the electrochemical sodiation of the Pb composite electrode gives a volume expansion of up to ~365% upon the formation of $Na_{15}Pb_4$.[27] This significant volume expansion makes the cycle life of Pb-based composite electrodes work less than 20 cycles,[28] far from the industrially acceptable level, which renders its practical utilization.

It is well-recognized that the volume change is directly linked to the phase transformations that occur during the electrochemical (de-)sodiation. The sodiation mechanisms of Pb anodes remain poorly understood with only a few works being published over the years. Jow, et al. (1987), for the first time, reported that the alloying of Pb with Na occurs in four steps, leading to the formation of four distinct Na-Pb phases, i.e., $NaPb_3$, $NaPb$, Na_5Pb_2, and $Na_{15}Pb_4$.[27] The final sodiation product of Pb is also confirmed by Komaba, et al. that the initial sodiation capacity of ~480 mAh·g^{-1} matches ideally with the one calculated based on the atomic ratio of $Na_{15}Pb_4$.[29] However, a recent study, which comprehensively explored the Na-storage mechanisms of Pb thin film electrodes using in situ X-ray diffraction (XRD) technique, reveals that the electrochemical sodiation of Pb does not completely follow the Na-Pb phase diagram: The intermediate α-Na_9Pb_4, with a similar structure to Na_9Sn_4, is formed during the sodiation rather than the earlier suggested Na_5Pb_2 phase.[28] A similar outcome was also reported later by Ali Darwiche et al.,[23] in which *operando* XRD measurements verified the presence of $NaPb_3$, $NaPb$, Na_9Pb_4, and $Na_{15}Pb_4$ phases during the sodiation process of the electrode with microsized Pb particles as the active material. Again, no crystalline Na_5Pb_2 phase was detected. Regardless of whether Na_5Pb_2 or Na_9Pb_4 is a thermodynamically stable phase at room temperature, there is almost no doubt that the electrochemical sodiation of Pb forms different successive intermetallic phases. Given that these Na-Pb phases (e.g., $NaPb_3$, $NaPb$, Na_9Pb_4/Na_5Pb_2, $Na_{15}Pb_4$) have different crystal structures and mechanical properties (e.g., elastic modulus, shear modulus, etc.), the reversibility of each phase transformation pair should also vary. Therefore, identifying which phase transformation pair plays a greater impact on the electrochemical performance is essential to assess whether solid, non-composite, Pb can potentially be a reliable SIB anode in the future.

Here we use metallic Pb foils as the model electrodes, because of the simple monolithic design[30] and low cost.[31] Additionally, the foil electrode design presents alternative constraints compared to the composite electrodes, whereby expansion and contraction are expected to be buffered to a varying degree by ductile, unreacted Pb. The Na storage behavior of the Pb electrode in a foil architecture is systematically evaluated thereafter, building fundamental insights into the phase transformations, and discussing their role in electrode reversibility and stability. By deliberately mitigating or circumventing the problematic phase transformations, the prolonged cycle life of Pb electrodes in SIBs could be realized.

Materials and Methods

The chemicals and materials used in the work include: Pb foil (99.99%, Anhui Zhengying Technology Co., Ltd.), Na metal (99.9%, Sigma-Aldrich), Sodium Vanadium Phosphate $Na_3V_2(PO_4)_3$ (NVP) cathode powder (D50: 20 μm, 97%, containing 3% carbon, Advanced Materials and Lab Equipment Supplier), polyvinylidene fluoride (PVDF) powder (average M_w ~540,000 by GPC, Sigma-Aldrich), N-methyl-2-pyrrolidinone (NMP) (99%, Sigma-Aldrich), carbon black powders (Graphite and SuperP C45, TIMCAL C-NERGY^{TM}, IMERYS), glass fiber separator (Whatman®), 1 M $NaClO_4$ in ethylene carbonate (EC) and propylene carbonate (PC) with a volume ratio of 1:1 (DoDoChem, China), Dimethyl carbonate (DMC) (≥99%, acid<10 ppm, H_2O<10 ppm, Sigma-Aldrich), 15 μm-thick Al foil current collector, 2032-type coin cell components (case, spring, and spacer, MTI Corp).

Coin-cell assembly.—Pb//Na half-cells were prepared by pairing the 30 μm-thick Pb foil (12 mm in diameter) with the Na metal in an argon-filled glovebox (H_2O < 0.1 ppm, O_2 < 0.1 ppm). The two electrodes are separated by a glass fiber separator and the electrolyte used here is 1 M $NaClO_4$ in EC: PC = 1:1. The NVP//Pb full cells were assembled in the same way, but the Na counter electrode is used to replace the NVP cathode. To prepare the cathode, PVDF powder was dissolved in NMP solvent to make a 5 wt% PVDF solution. Later, the NVP powder, carbon black powders, and PVDF in a mass ratio of 85%, 5%, and 10% were weighed and mixed in a plastic jar at 1500 rpm for 25 min. The obtained slurry was then coated on the Al current collector and dried in a vacuum oven at 90 °C for ≥24 h. The dried NVP sheet was pouched into disks with a diameter of 12 mm for cell assembly. The mass loading of the NVP cathode is ~1 mg·cm^{-2}. As for the anode, to effectively avoid any catalytic reaction of Pb with the electrolyte, a piece of Na metal is pressed onto the Pb foil electrode for approximately 40 min before cell assembly, such that a new interface between the electrode and electrolyte is formed. The open-circuit voltage of the full cell with the NVP cathode and presodiated Pb foil anode is measured to be ~2.5 V at first and drops to ~2.4 V after the 10 h rest.

Electrochemical measurements.—All the electrochemical measurements in this work were done at room temperature using the LAND battery testing system (LANHE, China). For the Pb//Na half-cells, an initial current of −0.5 mA was applied until 0.8 V (vs Na/Na$^+$) was reached to rule out the catalytic reactions occurring at relatively high potentials on the surface of the Pb electrode.[28] After that, the cells were discharged and charged at the constant current of 0.1 mA (~C/177, based on the theoretical capacity of $Na_{15}Pb_4$) at five different cutoff voltages: 0.001–0.8 V (Pb/$Na_{15}Pb_4$), 0.4–0.8 V (largely Pb/$NaPb_3$), 0.15–0.45 V (largely $NaPb_3$/NaPb), 0.09–0.35 V (largely $NaPb/Na_9Pb_4$), and 0.001–0.2 V (largely $Na_9Pb_4/Na_{15}Pb_4$) vs Na/Na$^+$. The NVP//Pb full cells were cycled in the voltage window including the (de-)sodiation plateau voltage of Pb//Na and NVP//Na half cells. The electrochemical impedance spectroscopy (EIS) measurements were done on the Pb//Na cells before the sodiation, and sodiating to 0.25 V, 0.15 V, 0.1 V, and 0.001 V vs Na/Na$^+$ at room temperature. The frequency range for the measurement is 100 kHz-10 mHz with a voltage amplitude of 5 mV.

Materials characterization.—Ex situ X-ray diffraction (XRD) characterization for the Pb electrodes during the initial (de-)sodiation process was carried out by the X-ray diffractometer (D8 ADVANCE, BRUKER) with Cu Kα radiation at 5 degrees per minute in 2θ angle range of 20°−80°. To minimize the oxygen interference, the (de-)sodiated Pb electrodes were sequentially disassembled, rinsed three times with DMC solvent to try to remove the surface salt, and sealed in an airtight holder in an argon-filled glovebox before the XRD measurements. The morphology of the Pb foil electrodes at different depths of discharge (DoD) or state of charge (SoC) was revealed by field-emission scanning electron

microscopy (Zeiss-Supra 55VP-FE-SEM). The sample preparation for SEM followed the same way as that for the XRD tests. To reduce the air exposure, we sealed the samples in two vacuum bags before taking them into the SEM chamber.

Results

Initial sodiation-desodiation of Pb foil anodes.—Fig. 1a shows the typical sodiation-desodiation (or discharge-charge) profile of the Pb foil electrode cycled at 0.1 mA ($\sim$C/177 considering the formation of $Na_{15}Pb_4$). As soon as the sodiation current is applied, the surface potential of the electrode rapidly drops to $\sim$0.25 V (vs Na/Na$^+$) and then slowly rises to $\sim$0.3 V. This potential difference of $\sim$50 mV was defined by Wang et al. as the nucleation potential,[32] which are regularly observed in alloy anodes for LIBs/SIBs.[33] Three distinct potential plateaus at $\sim$0.3 V, $\sim$0.12 V, and $\sim$0.08 V vs Na/Na$^+$ are observed one after another, delivering a specific capacity of $\sim$480 mAh·g^{-1} ($\sim$1170 mAh·cm^{-3}) after a sodiation until 0.001 V vs Na/Na$^+$, consistent with previous reports.[23,28] By extracting the capacities contributed by each potential plateau, it is found that these capacities match the ones upon the formation of NaPb$_3$, Na$_9$Pb$_4$/Na$_5$Pb$_2$, and Na$_{15}$Pb$_4$ based on calculations. When

the current direction is inverted, the potential curve exhibits four desodiation potential plateaus at $\sim$0.15 V, $\sim$0.28 V, $\sim$0.38 V, and $\sim$0.5 V vs Na/Na$^+$, indicating four Na-Pb two-phase equilibrium regions. Different from the smooth sodiation curve, the desodiation one is significantly noisier, especially for the second and fourth potential plateaus. The noisy desodiation curve was also reported in the Sn electrode,[34] which might be associated with the loss of electrical contact caused by mechanical damage. After the desodiation to 0.8 V vs Na/Na$^+$, a specific capacity of $\sim$450 mAh·g^{-1} is obtained, corresponding to $\sim$93% ICE of the initial cycle.

To examine whether the Na-Pb phases exist, and assess their reversibility, XRD tests were performed systematically on the initial cycle of the Pb foil anode. As shown in Fig. 1b, prior to the sodiation (dot #1 in Fig. 1a), the diffractogram of the pristine Pb foil (#1 in Fig. 1b) is fitted to the crystalline Pb (PDF #01-072-22773), and the Pb oxides (PDF #00-035-1482). As the sodiation capacity proceeds to $\sim$1.42 mAh·cm^{-2} (dot #3 in Fig. 1a), the diffractogram generally remains the same except for some additional minor reflections/peaks that likely correspond to the Na-Pb oxides (#3 in Fig. 1b). No obvious peaks related to Na-Pb phases (i.e., NaPb$_3$) are detected. With further sodiation to a capacity of $\sim$4.43 mAh·cm^{-2} (dot #4 in
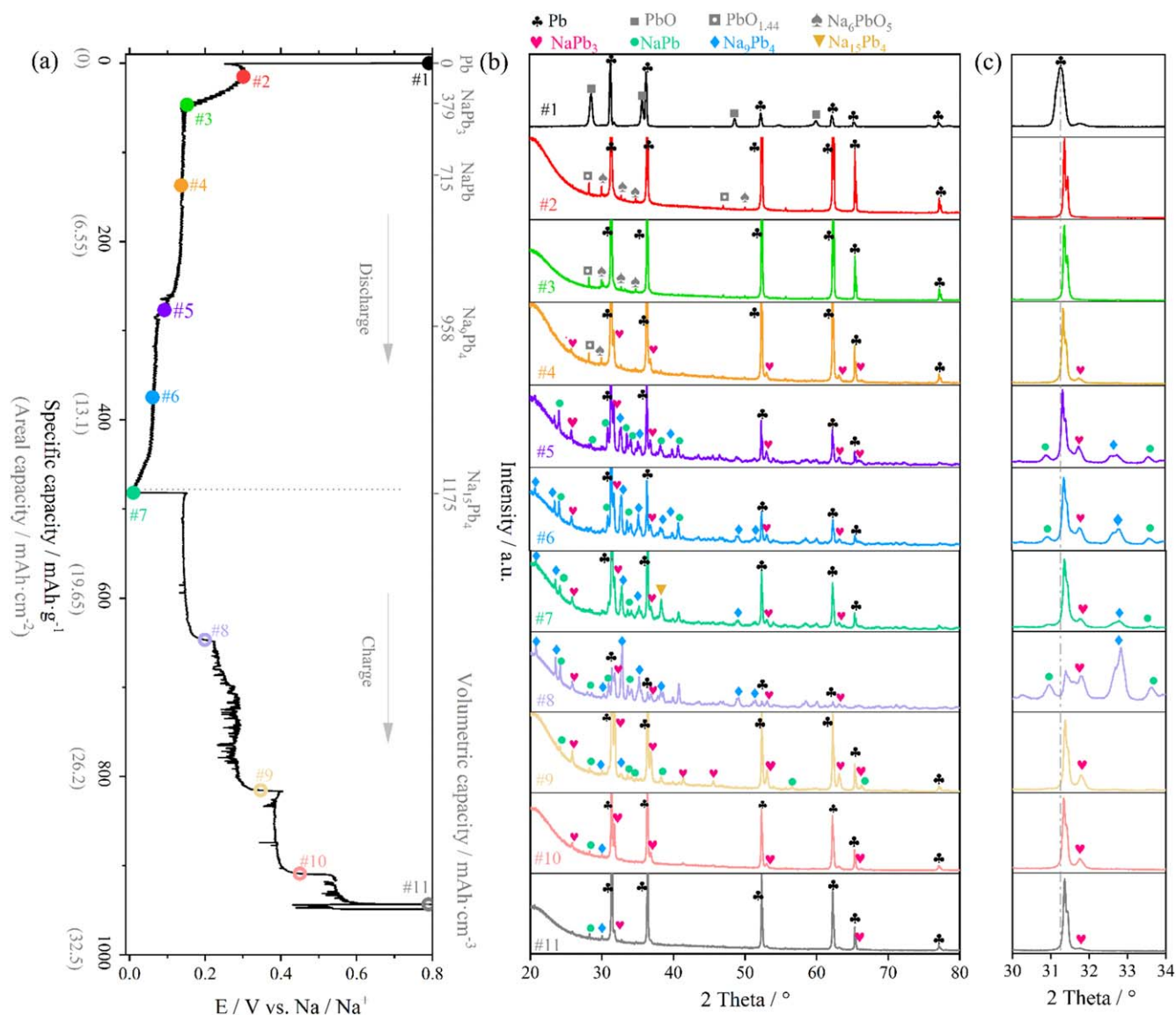

Figure 1. (a) The initial galvanostatic profile of a Pb//Na half-cell at a C-rate of 0.1 mA (12 mm electrode disk). (b) The XRD diffractograms of the Pb electrodes at different sodiation or desodiation states, which are highlighted by the colored dots in Fig. 1a. (c) The enlarged XRD diffractogram in $2\theta = 30°$–$34°$ for Fig. 1b.

Fig. 1a), the diffraction peaks corresponding to the $NaPb_3$ phase appear, although the peaks of crystalline Pb remain the most prominent (#4 in Fig. 1b). No diffraction peaks referring to the higher-ordered crystalline Na-Pb phases (e.g., NaPb, Na_9Pb_4) are observed at this point. After the sodiation capacity reaches ∼10.4 mAh·cm^{-2} (dot #5 in Fig. 1a), the diffraction peaks corresponding to the higher-ordered phases of NaPb and Na_9Pb_4 finally appear (#5 in Fig. 1b), in addition to the remaining $NaPb_3$ and Pb diffraction peaks. Even after the deep sodiation to 0.001 V vs Na/Na$^+$ (dot #7 in Fig. 1a) at this small current, the typical diffraction peaks corresponding to pristine Pb remain (#7 in Fig. 1b). Taking a closer look at the strong peak at around 31.4° (Fig. 1c), which agrees with the standard ones of the Pb phase, one can see that they seem to shift slightly towards a higher 2θ angle with the increasing sodiation depth (highlighted by the gray dashed line in Fig. 1c). One explanation for this peak shift is related to mechanical strain. The localized volume expansion caused by inhomogeneous sodiation compresses the neighboring unsodiated Pb grains, resulting in a decreased plane distance and thereby shifting the diffraction peak rightward (Bragg's law). Another possibility may have something to do with the thick Pb foil samples. As the phase boundary moves into the electrode, the diffraction from the Pb phase moves deeper into the electrode along the z-axis (i.e., a longer pathway for the X-ray). In this way, when the detector gets the diffracted X-ray from the sample, it may have already rotated to a slightly higher angle degree (given the scanning speed of 5°/min), thereby resulting in a larger measured 2θ, i.e., a rightward shifting peak. In either case, future studies are warranted.

Moreover, no strong evidence proves the presence of $Na_{15}Pb_4$, i.e., only one typical diffraction peak at $2\theta \approx 38°$ may be contributed by the $Na_{15}Pb_4$ phase (PDF #03-065-3168) while others can hardly be distinguished due to the low peak intensity and the peak overlapping. It is noted that the diffractogram of the deeply sodiated Pb foil (to 0.001 V) also exhibits the features of a mixture of crystalline $NaPb_3$, NaPb, and Na_9Pb_4. The XRD results suggest that some of the phase transformations during sodiation may occur simultaneously rather than sequentially, otherwise, peaks corresponding to the three Na-Pb phases (i.e., $NaPb_3$, NaPb, Na_9Pb_4) should not have been concurrently observed to such an extent.

When the electrode is desodiated to ∼0.2 V vs Na/Na$^+$ (dot #8 in Fig. 1a), a typical diffraction peak at ∼38.2° that is likely corresponding to $Na_{15}Pb_4$ diminishes, and more peaks appear simultaneously, which agrees with the typical diffraction peaks of Na_9Pb_4 reported by Ellis et al.[28] (#8 in Fig. 1b). The desodiation of the Pb foil anode to 0.35 V vs Na/Na$^+$ (dot #9 in Fig. 1a) results in the absence of some typical diffraction peaks that may originate from Na_9Pb_4 (e.g., at 23.5°, 35°, and 49°), and the presence of new peaks that may be contributed by NaPb (e.g., at 38°, 56°, and 66.5°) and $NaPb_3$ (e.g., at 42° and 45°) (#9 in Fig. 1b). For the electrode desodiated to 0.45 V vs Na/Na$^+$ (dot #10 in Fig. 1a), the prominent features of the diffractogram are consistent with those of $NaPb_3$ and Pb from the PDF cards #03-065-3283 and #01-072-22773, while some small peaks that are in line with standard peaks of Na_9Pb_4 and NaPb phases are also visible (#10 in Fig. 1b). When the electrode is desodiated to 0.8 V vs Na/Na$^+$ (dot #11 in Fig. 1a), the main diffraction peaks of the diffractogram are in line with those of the
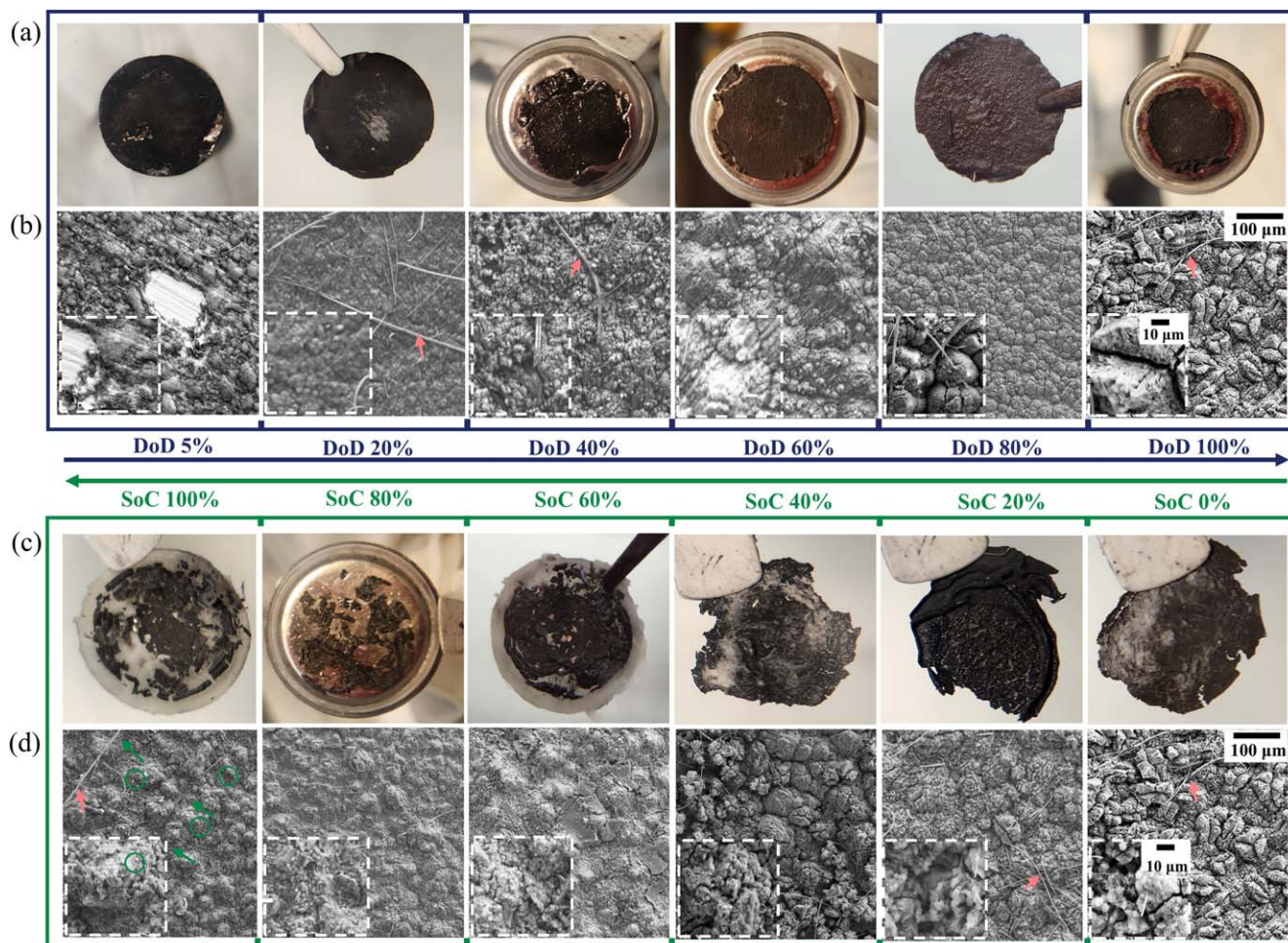
Figure 2. (a) (c) The photographic images and (b) (d) the corresponding SEM images (bottom) of the Pb foil electrode surface at different sodiation (or desodiation) states during the initial cycle. It is noted that the photographs were taken on the rinsed electrode sample at different DoD or SoC in the glovebox. The cracks and voids are highlighted in green arrows and circles, while the residue glass fiber on the electrode surface is marked in red arrows.

metallic Pb phase, with minor peaks that may originate from NaPb$_3$, NaPb, or Na$_9$Pb$_4$ phases (#11 in Fig. 1b).

To summarize, multiple Na-Pb intermetallic phases are involved in the sodiation of the Pb foil electrode. These phases are suggested to be NaPb$_3$ NaPb, Na$_9$Pb$_4$/Na$_5$Pb$_2$, and Na$_{15}$Pb$_4$ based on the electrochemical data and the previous reports on Pb micro-sized particles[23] and thin films.[28]

Surface morphology of Pb foil anodes.—The surface morphology changes of the Pb foil anodes during the initial cycle are characterized by taking photographic and scanning electron microscopy (SEM) images. Figure 2 shows the photographic images and the corresponding SEM images taken at different states of (dis-) charge. Upon a 5% DoD (~0.85 mAh), the electrode is mostly covered by a sodiated layer and maintains its disk geometry (Fig. 2a). With a deeper sodiation, i.e., 20% DoD, the electrode surface and shape do not change significantly by eye observation. The electrodes with ⩾ 40% DoD, on the contrary, can hardly maintain their integrity and may break into parts after disassembly. Since the electrode with 80% DoD seems to hold its overall structure, it is suggested that the external force coming from the disassembly of the coin cell may partly be responsible for the structure collapse of the electrodes with 40%, 60%, and 100% DoD. Low- and high-magnification SEM images of the electrode at the same DoD are provided in Fig. 2b. At 5% DoD, the sodiated layer grown on the electrode surface exhibits a shape of emerging spherical protrusions while the unsodiated portion retains the same appearance as its pristine state with the rolling trace (Fig. S1). When the DoD is higher, the features of the electrode surface do not seem to change significantly, and no obvious cracks are found in the chosen observation region. However, when the DoD reaches 80%, some small cracks on top of the protrusions (high-magnification SEM) can be observed. The electrode with 100% DoD becomes more catastrophic since the structure of protrusions opens up, leading to severe cracking.

The EIS measurements (Fig. S2) of the Pb foil electrode sodiated to different potentials (i.e., 0.25 V, 0.1 V, and 0.001 V vs Na/Na$^+$) were also conducted to characterize the solid electrolyte interface (SEI), which may not be revealed by SEM. The capacitive semicircle at high frequencies, generally dominated by the charge transfer resistance, becomes notably smaller as the sodiation proceeds from 0.25 V to 0.15 V, but then remains upon further sodiation until 0.001 V, indicating a relatively stable SEI layer below 0.15 V vs Na/Na$^+$.

From the photographic images (Fig. 2c), the electrode with 20% SoC completely loses its disk shape. With a higher SoC, the electrode seems to follow a trend that the higher the SoC, the lower

the electrode integrity is. When the SoC is beyond 60%, the electrode breaks into parts after disassembly. This structural damage may partly explain the noisy potential profile during desodiation (Fig. 1a). The SEM observations (Fig. 2d) show that with the increasing SoC, the cracked protrusions on the electrode surface do not seem to be as evident as those in 0% SoC (i.e., 100% DoD). For instance, only some smaller cracks can be identified in the electrode surface at 100% SoC (arrow in Fig. 2d). Meanwhile, the surfaces of the electrodes with ⩾ 40% SoC appear to be flatter, evidenced by the island-like protrusions that are not as compact, and the surface of the fully desodiated electrode seems to become mossy (highlighted by circles in Fig. 2d). In addition, it should be noted that some glass fibers (marked in the red arrow in Figs. 2b and 2d) are still observed on the electrode surface, although the electrode samples were rinsed using pure DMC solvents three times after the disassembly. This might be related to the stack pressure, which causes some glass fibers tightly attached to the rough surface of the electrode.

Reversibility of different phase transformations in Pb foil anodes.—Theoretically, the full sodiation of Pb upon the formation of Na$_{15}$Pb$_4$ will give rise to a volume expansion of ~365%, which could induce huge mechanical strain in the electrode, therefore leading to mechanical damage like cracking (as shown in Figs. 2b and 2d) and pulverization.[23] As anticipated, the galvanostatic charge-discharge (GCD) results (Figs. 3a and 3b) show that the Pb foil electrode cycled within 0.001–0.8 V stops functioning after only 3 cycles, and the failure mechanisms have not been reported yet. Taking a close look at the GCD curves, one can see that there are four potential plateaus during the second sodiation, in contrast to three in the initial sodiation. The second desodiation becomes even more catastrophic with a significantly noisier potential profile.

Identifying which phase transformations are largely responsible for the electrode failure and strategically eliminating their negative impact from the electrochemical cycling is essential to prolong the cycle life of Pb foil electrodes. Here we systematically explore the reversibility of each pair of phase transformations (both directions) by controlling the cutoff voltages during GCD cycling. Figures 4a–4d shows the voltage profiles of Pb foil electrodes cycled within 0.4–0.8 V, 0.15-–0.45 V, 0.09–0.35 V, and 0.001–0.2 V vs Na/Na$^+$, aiming to examine Pb/NaPb$_3$, NaPb$_3$/NaPb, NaPb/Na$_9$Pb$_4$, Na$_9$Pb$_4$/Na$_{15}$Pb$_4$, respectively, in isolation. The electrodes after the initial cycle deliver the areal capacities of ~1.1 mAh·cm^{-2} (~33.6 mAh·g^{-1}), ~2.4 mAh·cm^{-2} (73.3 mAh·g^{-1}), ~4.8 mAh·cm^{-2} (146.6 mAh·g^{-1}), and ~7 mAh·cm^{-2} (213.8 mAh·g^{-1}) for these four pairs of phase transformations, respectively, which are in line with their theoretical capacities. In general, cycling stability should be reversely correlated to the depth of sodiation because a deeper sodiation induces higher
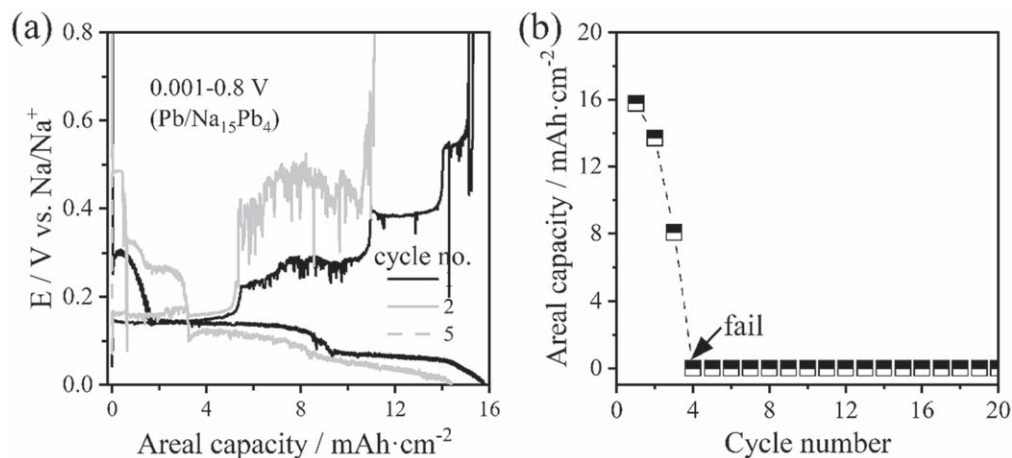

Figure 3. (a) The galvanostatic profiles of the Pb foil electrode during the 1st, 2nd and 5th cycles at 0.1 mA (12 mm electrode disk) with a potential range of 0.001–0.8 V. (b) The cycling performance of the Pb foil electrodes under the same charge-discharge conditions.
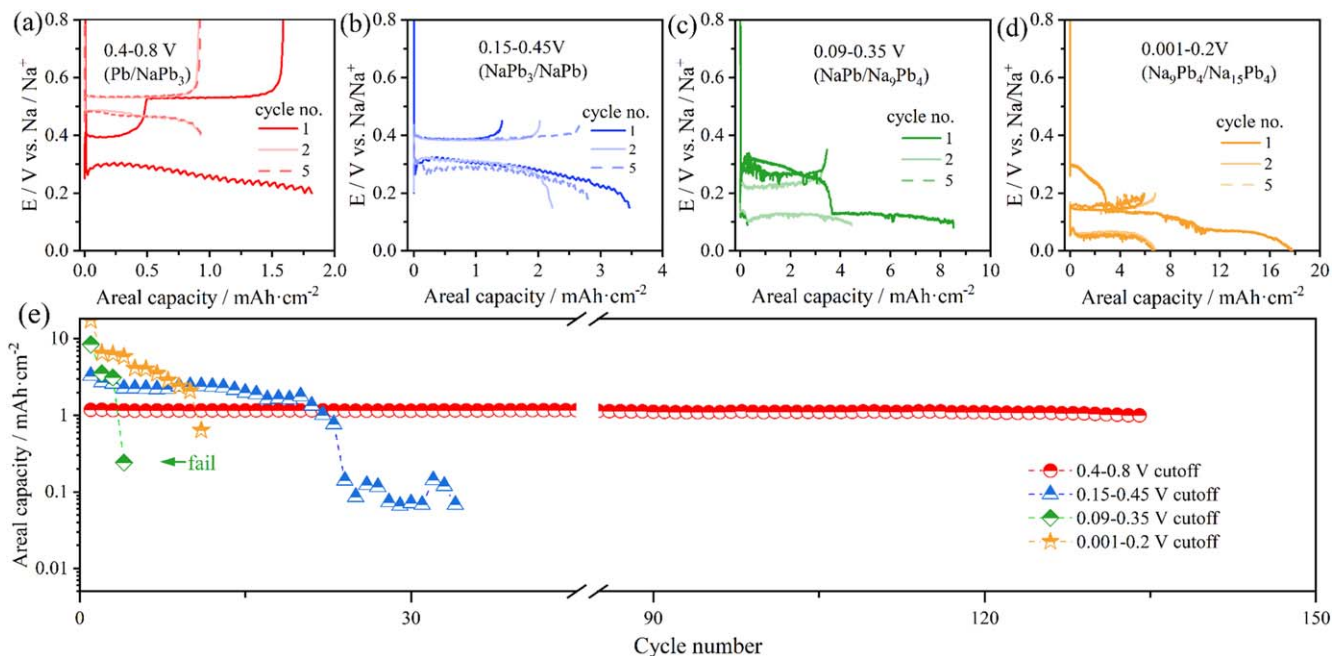
Figure 4. The galvanostatic profiles of the Pb foil electrode during the 1st, 2nd and 5th cycles, obtained from cycling at 0.1 mA with different voltage windows: (a) 0.4–0.8 V, (b) 0.15–0.45 V, (c) 0.09–0.35 V, (d) 0.001–0.2 V. (e) The capacity retention for the cycling within the same cutoff voltages.

volume change considering the initial geometry of the Pb foil. As anticipated, the cycling data of the first three phase transformations (i.e., $Pb/NaPb_3/NaPb$) agree with the trend described just before (Fig. 4e). For instance, the electrode cycled within 0.4–0.8 V (largely $Pb//NaPb_3$) gives the best cycling performance, maintaining ~86% of its initial capacity after 130 cycles. Specifical attention should be paid to the last two pairs of the phase transformations where the trends no longer stand. Cycling within 0.09–0.35 V (i.e., largely $NaPb/Na_9Pb_4$) shows the fastest capacity degradation: It can merely survive 3 cycles (same as full sodiation cycling in Fig. 3) before its failure (i.e., 10% of the initial capacity). On the contrary, the electrode cycled between 0.001 and 0.2 V shows a better lifetime of approximately 12 cycles. These cycling tests of the electrode at the two cutoff voltages which were repeated a couple of times (Figs. S3–S4), can well support the unexpected trends. The poorer reversibility of 0.09–0.35 V cycling indicates that other factors in addition to the volume change should also play a critical role in the phase transformations.

SEM images (Fig. S5) of the electrode after different cycles within the above-mentioned voltage windows may provide implications on why these phase transformations perform differently. In the case of 0.4–0.8 V, and 0.15–0.45 V, both electrode surfaces are relatively flat, and retain some trace of calendaring after 1st cycle (Figs. S5a and S5b). Moreover, no evident electrode destruction is observed after 15 cycles in the above-mentioned two cases: No obvious cracks, voids, or pulverization. This structural stability can largely explain the better cycling stability of these two pairs of phase transformations. Differently, some signs of mechanical damage for the electrode are observed in the other two cycling scenarios with deeper sodiation, i.e., between 0.09–0.35 V and 0.001–0.2 V (Figs. S5c–5d). Particularly for the former case, many voids and small cracks seem to appear on the electrode surface after the 5th cycle (Fig. S5c).

Microstructural changes of Pb foil anodes during the problematic phase transformations.—To further understand the poorest reversibility of the $NaPb/Na_9Pb_4$ phase transformations, the morphological changes of the electrode in the 1st and 2nd cycling between 0.09–0.35 V vs Na/Na^+ are characterized (Fig. 5). The first sodiation to 0.09 V (Fig. 5a) gives rise to some cracks on the protrusions, although the overall electrode integrity is maintained.

After the subsequent desodiation to 0.35 V, the electrode surface exhibits porous and mossy features (circles in Fig. 5b). Despite no study reporting the formation of the voids in the desodiated Pb, it seems not surprising since many alloy electrodes, e.g., Sn(-Li), Si (-Li), and Al(-Li), are reported to be porous after selective dealloying processes.[33,35,36] As the electrode is sodiated to 0.09 V for the second time, most voids remain (Fig. 5c), which appear to become larger when desodiating to 0.35 V (Fig. 5d). These physical damages could partly explain the poorest cyclability of the Pb foil electrode in the voltage range of 0.09–0.35 V.

Cycling performance of full cells with Pb foil anodes.—Given the problematic transformations, the Pb foil electrode is suggested to be utilized by largely cycling $Pb/NaPb_3$ or $Pb/NaPb$, depending on the capacity contributed by the cathode. Stable long-term cycling is a prerequisite to the practical application of rechargeable batteries. Here we evaluate the cycling stability of the Pb foil electrode in a full cell configuration with NVP as the cathode (ca. 0.09 $mAh\cdot cm^{-2}$). Noteworthy, to minimize the catalytic effect of Pb, a small amount of sodium is pre-stored in the Pb electrode surface layer (i.e., chemical presodiation), causing an open circuit voltage of ~2.4 V for the NVP//Pb full cells (vs ~0.6 V for the cell with the NVP cathode and a fresh Pb anode). The galvanostatic profiles of NVP//Na, Pb//Na, and NVP//Pb, are provided in Fig. 6a, of which the NVP//Pb full cell is characterized to have two flat and long plateaus at ~3.2 and ~2.9 V for charge and discharge, respectively. Figure 6b shows the 1st, 5th, 50th, 100th, 200th, and 300th GCD curves of the NVP//Pb full cell within the voltage range of 2.2–3.6 V at 0.15 $A\cdot g\text{-}NVP^{-1}$ (~0.15 $mA\cdot cm^{-2}$). Furthermore, the cycling performance of the NVP//Pb full cell (Fig. 6c) displays that at 0.15 $A\cdot g\text{-}NVP^{-1}$, the reversible capacity of the cells gradually drops to ~65 $mAh\cdot g\text{-}NVP^{-1}$ after 300 cycles, corresponding to approximately 60% of the initial capacity.

Discussion

Clarification of Na-Pb intermetallic phases during sodiation.—Here our electrochemical results are integrated with the published Na-Pb phase diagram to clarify the intermetallic phases during the sodiation. From Fig. 7, in general, the intermetallic Na-Pb phases detected by XRD largely agree with the binary phase diagram[28] but
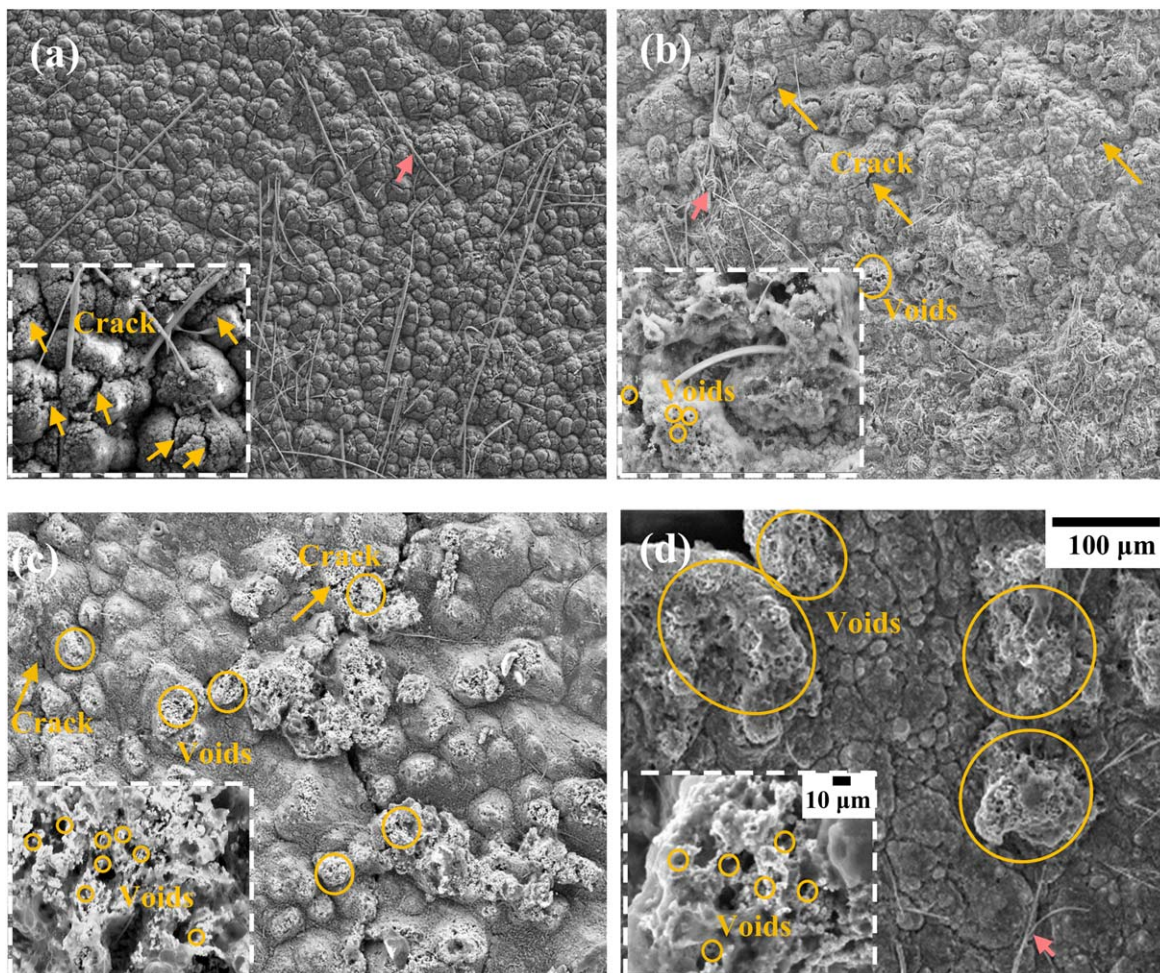
Figure 5. SEM images of the Pb foil electrodes at different states when limited to the problematic phase transformations: (a) 1st sodiation to 0.09 V, (b) 1st desodiated to 0.35 V, (c) 2nd sodiation to 0.09 V and (d) 2nd desodiation to 0.35 V. Cracks are denoted by yellow arrows while voids are denoted by yellow circles. The glass fibers remaining on the electrode surface are also marked by red arrows.

the simultaneous formation is suggested instead of sequential, explaining why the single-phase region (i.e., #7) does not solely exhibit the diffraction peaks that correspond to the specific phase.

Upon the initial sodiation (the shaded region near the origin in Fig. 7), the Pb electrode is probably saturated with Na to form a solid solution with the maximum Na content of ~2 at% at room temperature while maintaining the original crystal structure, although the electrolyte breakdown and sodiation of the thick surface Pb oxides should not be neglected. The Pb (Na) solid solution should be limited to a very thin layer on the electrode surface considering that Na diffusion is extra slow in pristine Pb foil (including Pb oxides), i.e., $\sim 10^{-13}$ cm$^2 \cdot$s^{-1}.[37] As the sodiation continues, Na atoms keep accumulating on the electrode surface until the nucleation of the new NaPb$_3$ phase (the potential dip highlighted by an arrow in Fig. 7).

Although the endpoint of the first potential plateau (#3 in Fig. 7) is located around the NaPb$_3$ region, the XRD results do not seem consistent (#3 in Fig. 1b). This mismatch is acknowledged by the inhomogeneous nucleation of Na-Pb phases, which is often observed in alloy electrodes in Li- and Na-based systems.[38–40] It is reported that subsequent phase transformations tend to occur along certain crystal planes or orientations in alloy electrodes.[41–44] Furthermore, sluggish kinetics (i.e., the slow Na diffusion in Pb) are suggested to be responsible, such that over-sodiation may occur at the positions (e.g., phase boundaries, dislocations, etc.) that are accidentally not hit by the X-ray. It should be noted that the β phase (i.e., 28 at% to 35 at% Na) indicated by the phase diagram published in 1968[45] is

not observed electrochemically, nor in the previous reports,[23,28] thereby is intentionally excluded from Fig. 7.

On the first half of the second sodiation plateau (#4 of Fig. 7) where a coexistence of NaPb$_3$ and NaPb is expected, the diffraction peaks corresponding to NaPb$_3$ are detected. The lattice parameters of the NaPb$_3$ phase are refined from the XRD results to be $a=b=c=0.488$ nm, consistent with the reported ones,[23] further supporting that NaPb$_3$ is the first sodiation phase other than the β phase presented in the phase diagram.[28] This potential plateau terminates with the stoichiometry of Na$_9$Pb$_4$ (#5 in Fig. 7), where all the diffraction peaks referring to NaPb$_3$/NaPb/Na$_9$Pb$_4$ are observed. The simultaneous phase formation may be caused by the different kinetical behaviors of each phase, akin to the sodiation of Ge,[11] but specific investigations are required to further quantify to what extent this is happening. As indicated by the phase diagram, the presence of Na$_5$Pb$_2$ remains debatable. An early study claimed that Na$_5$Pb$_2$ is formed by melting Na and Pb with identical atomic ratios but without the support of XRD results.[27] On the contrary, Obravoc et al. and Derwiche et al. confirmed the presence of Na$_9$Pb$_4$ instead of Na$_5$Pb$_2$, after sodiating a Pb electrode by in situ XRD technique.[23,28] Given that the literature of Pb anodes remains largely limited, we try to shed light on the formation of Na$_5$Pb$_2$ by discussing the analogical Na$_5$Sn$_2$, which is reported to be metastable, and its formation seems to be suppressed electrochemically.[46]

The last potential plateau ends at a point where the atomic ratio of Na/Pb calculated from electrochemical data nicely agrees with that presented in the phase diagram. However, some stubborn
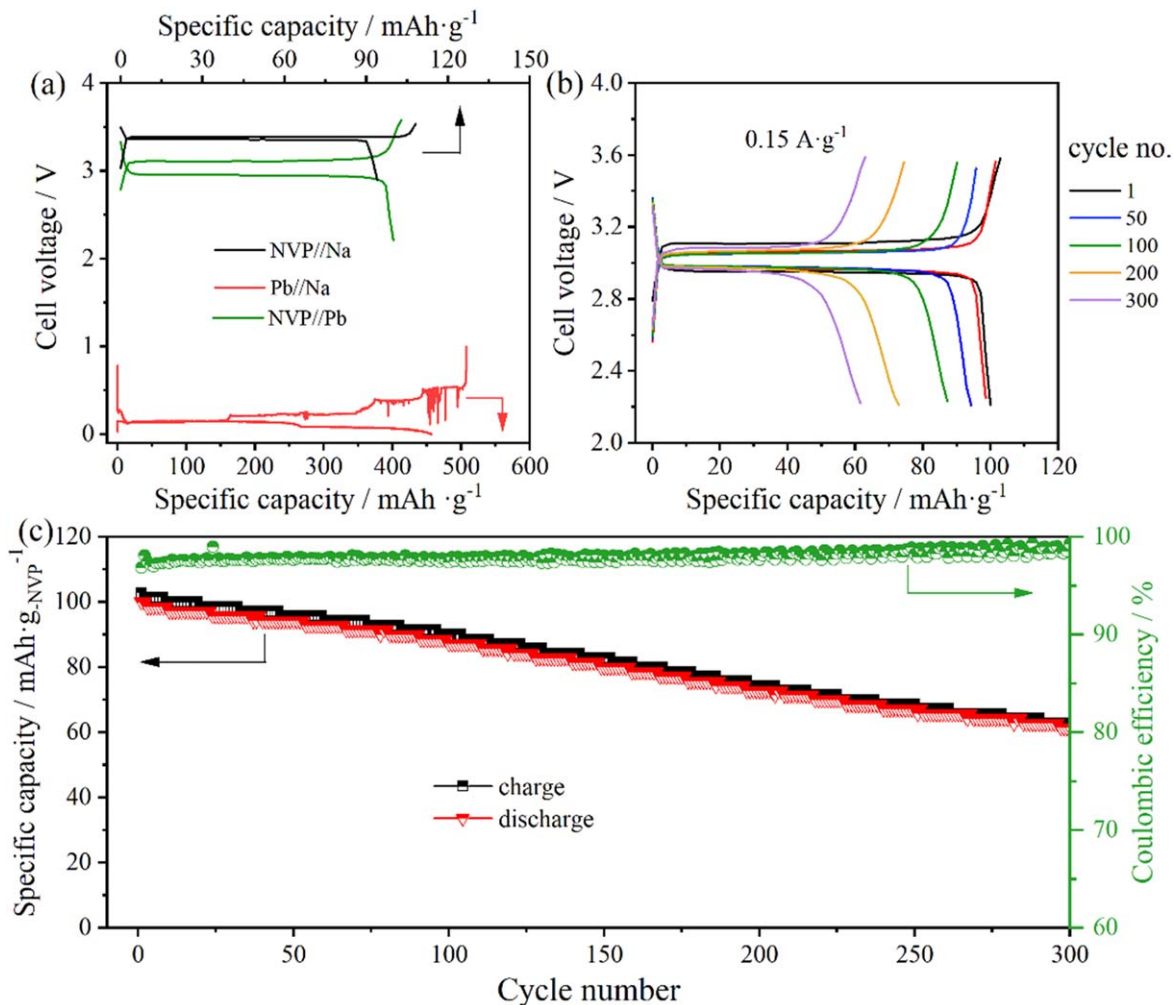
Figure 6. (a) The initial GCD curves of a Pb//Na half-cell, an NVP//Na half-cell, and a NVP//Pb full cell cycled at 0.1 mA (0.15 A·g-NVP^{-1}). (b) The 1st, 5th, 50th, 100th, 200th and 300th galvanostatic profiles and (c) the long-term cycling performance of NVP//Pb full cells at 0.15 A·g-NVP^{-1}.

regions are not fully sodiated to reach the $Na_{15}Pb_4$ phase, as indicated by the X-ray diffractogram (#7 in Fig. 1b). The incomplete sodiation of these regions may be restricted by the huge mechanical strain caused by the volume expansion that compresses the neighboring grains, subsequently shifting the sodiation potential towards a lower level, even below 0 V vs Na/Na$^+$.[47] This explanation can be evidenced by the minor peak shift of Pb toward a higher 2θ degree in the diffractogram (grey dashed line in Fig. 1c), which is characteristic of significant mechanical strain. Similar observations were also reported in other alloy electrodes, such as Al and Sn, in Li-based systems.[34] To summarize, from our XRD results of the simultaneous formation of multiple phases, the electrochemistry on Pb foil electrodes suggests that the overall electrode equilibrium during the initial cycle should be described as: $Pb \leftrightarrow NaPb_3$, ($NaPb$, Na_9Pb_4, $Na_{15}Pb_4$).

Impact of crystal structures on the electrode reversibility.—The sodiation of Pb induces a significant crystal rearrangement by forming multiple Na-Pb intermetallic phases, i.e., cubic $NaPb_3$, tetragonal $NaPb$, orthorhombic Na_9Pb_4, and cubic $Na_{15}Pb_4$. The different lattice parameters, which are summarized in Table I, can give rise to a change in unit cell volume and atomic interactions, thereby affecting the reversibility of these phase transformations.

The unit cell volumes of these phases are distinctively different due to Na incorporation. It is common that the shallower the sodiation/lithiation (i.e., less volume expansion), the better the reversibility is, which seems to hold true for the Na-Pb system as

well. However, we have already noted that the $NaPb/Na_9Pb_4$ and the $Na_9Pb_4/Na_{15}Pb_4$ transformation do not follow the trend. The former undergoes a lattice volume expansion of $\sim$115.3%, smaller than that of the latter ($\sim$142.1%) but exhibits worse reversibility (Fig. 4). This observation suggests that other factors either caused by or independent from the volume change are also governing the reversibility of the phase transformations. For instance, it is known that significant mechanical stresses can accumulate near the phase boundaries where the lattice mismatch is more pronounced.[48] This interpretation is consistent with the observation of the stubborn unsodiated regions discussed previously (Fig. 1b). As soon as the stress is too large to be accommodated, mechanical failures are expected at the phase interface, leading to electrode degradation.

Different atomic interactions are expected in each Na-Pb intermetallic phase due to the differences in the Pb-Pb ($\sim$0.313 nm in Pb) and the Na-Na ($\sim$0.364 nm in Na) bonds. The Pb-Pb bonds in pristine Pb exhibit weakly covalent characteristics: Four valence electrons of the Pb atom are shared with those of the neighboring ones to form the chemical bonds. The electronic structure and the smaller length make the Pb-Pb bonds quite strong. As Na is incorporated into Pb, the Pb atoms will be gradually surrounded by Na atoms, and thereby the Pb-Pb bonds will be replaced by the newly formed Na-Pb bonds. As we can see from Table I, the substitution of shorter Pb-Pb bonds by the Na-Pb bonds with larger bond lengths (i.e., roughly 0.3469 nm for $NaPb_3$ and 0.3550 nm for $NaPb$) could induce an elastic softening in Na-Pb upon the transformation from Pb to NaPb, indicating lower stiffness for both
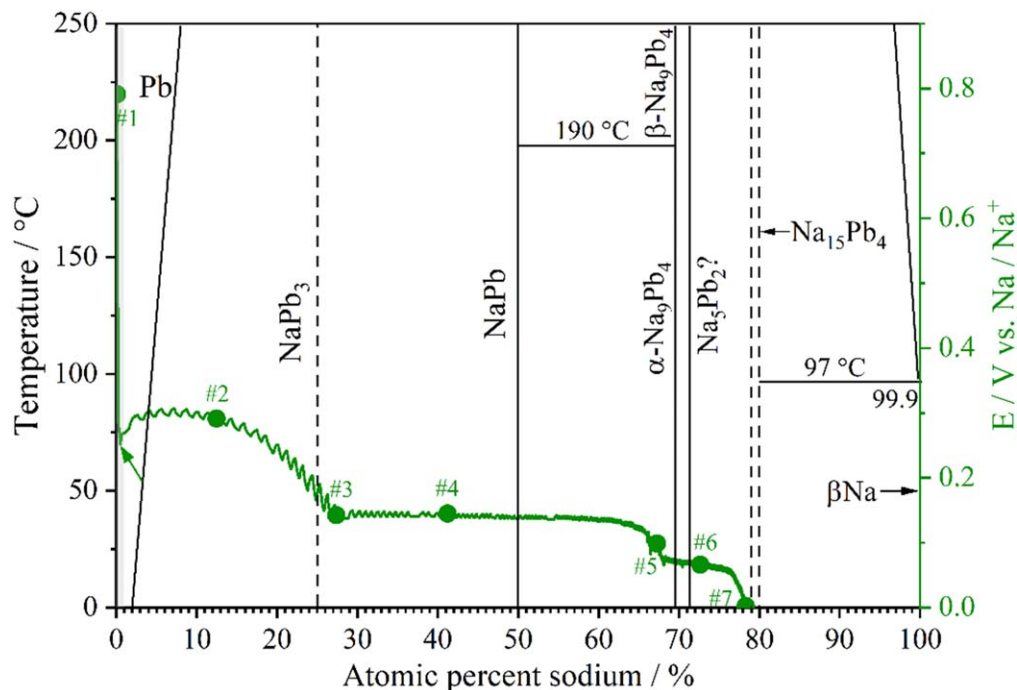
Figure 7. The initial discharge curve of Pb foil electrodes integrated with the Na-Pb phase diagram. It is noted that the highlighted dots here are consistent with those in Fig. 1a. The small oscillations in the galvanostatic profile are probably associated with the hardware limitations, as evidenced by Fig. S7 and the associated discussion.

Table I. The structural information of multiple Na-Pb intermetallic phases.

| Na-Pb phase | Crystal structure | Lattice parameters | | | Calculated volume expansion | Relative volume expansion to the prior phase | Pb-Pb bond length (nm) | Na-Pb bond length (nm) |
		a (nm)	b (nm)	c (nm)				
Pb	Cubic	0.4950	0.4950	0.4950	/	/	0.3130	/
NaPb$_3$[23]	Cubic	0.4873	0.4873	0.4873	~26.0%	~26.0%	0.3100	0.3469
NaPb[23]	Tetragonal	1.0580	1.0580	1.7740	~100.6%	~73.4%	0.3148	0.3550
Na$_9$Pb$_4$[28]	Orthorhombic	0.5471	0.945	3.0356	~215.9%	~115.3%	0.3141 or 0.2428	0.3000
Na$_{15}$Pb$_4$[23]	Cubic	1.3316	1.3316	1.3316	~358.0%	142.1%	/	0.3265

Note: The volume expansion and bond length are calculated based on the lattice parameters of the Na-Pb phases.

NaPb$_3$ and NaPb than Pb. However, further Na inclusion can cause stronger interatomic interactions, indicated by shorter Na-Pb bond lengths of Na$_9$Pb$_4$ (0.3000 nm) and Na$_{15}$Pb$_4$ (0.3265 nm). Consequently, the stiffness of both phases should be higher than that of NaPb$_3$, which can partly explain why the reversibility of NaPb/Na$_9$Pb$_4$ and Na$_9$Pb$_4$/Na$_{15}$Pb$_4$ is worse than that of Pb/NaPb$_3$ and NaPb$_3$/NaPb.

Impact of mechanical properties on the electrode reversibility.—The mechanical properties of each Na-Pb phase vary, evidenced by the DFT-calculated elastic, bulk, and shear moduli,[49] which are summarized in Table II. The ductility of each phase can be estimated by the ratio of bulk to shear modulus (B/G). It is found that Pb and NaPb$_3$ are relatively ductile, as indicated by higher B/G ratios of 3.19 and 3.90 respectively, whereas the higher-ordered Na-Pb phases (e.g., NaPb, Na$_{15}$Pb$_4$) tend to become more brittle, supported by the low B/G ratios (<2). Noteworthy, these mechanical moduli of the Na$_9$Pb$_4$ phase are absent, it is proposed that the Na-Sn system (e.g., Na$_9$Sn$_4$) may be used to shed light on the Na$_9$Pb$_4$ phase considering the similarity and the analogous nature of Na-Pb with Na-Sn alloys in physio-mechanical properties.[49] Also, the B/G ratio of the Na$_9$Pb$_4$ phase should not be distinctively different from that of

NaPb or Na$_{15}$Pb$_4$, although requiring further confirmation. As a result, for the Pb/NaPb$_3$ and NaPb$_3$/NaPb transformations, the ductile Pb and NaPb$_3$ can act as a buffer to accommodate the (de-)sodiation-induced mechanical stress by plastically deforming Pb or NaPb$_3$, thereby preventing the possible crack formation and enabling a long cycle life. In contrast, the NaPb/Na$_9$Pb$_4$/Na$_{15}$Pb$_4$ transformations may be more susceptible to cracking due to the brittleness of these phases, let alone their volume changes are more pronounced than those of Pb/NaPb$_3$/NaPb transformations. This interpretation is evidenced by the SEM observation of the electrode surface with no obvious crack or other mechanical damage (e.g., pulverization, loss of electrical contact, etc.) after 15 cycles when the electrode is limited to the Pb/NaPb$_3$/NaPb transformations (Figs. S5a–S5b). On the contrary, obvious cracks and voids are observed on the Pb foil electrode surface (Figs. 5 and S5c–S5d) during the cycling among NaPb/Na$_9$Pb$_4$/Na$_{15}$Pb$_4$. The formation of cracks and voids on the electrode surface exposes the fresh Pb to the electrolyte, facilitating secondary SEI formation and causing cyclic irreversible Na consumption, and thereby giving poor electrode reversibility.

The impact of diffusion kinetics on the electrode reversibility.—The Na diffusion kinetics also seem to play an important role in the
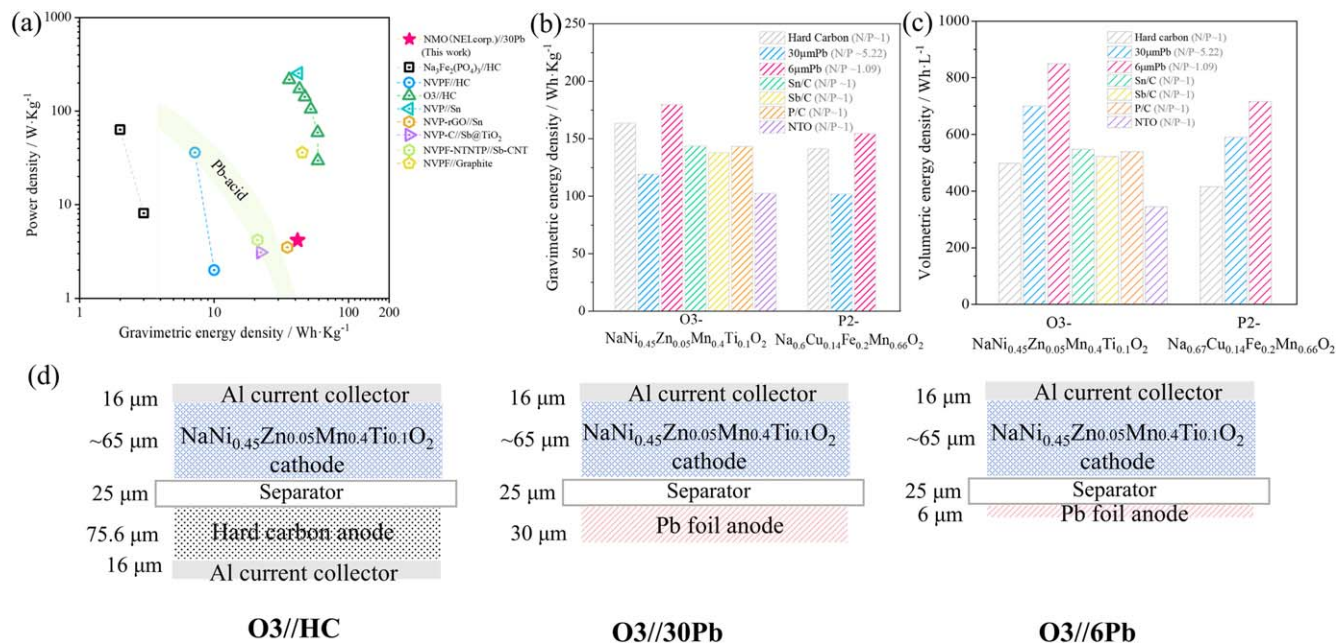
Figure 8. (a) The gravimetric Ragone plot of the Na-ion full cells with a 30 μm-thick Pb foil anode in comparison with the recently reported Na-ion cells. It is noted that the PABs energy density given here (green region) is based on the whole cell weight while other data are all based on the weight of the stack (including cathode, anode, current collector, separator, and electrolyte).[30](b) The calculated gravimetric and (c) volumetric energy density in comparison with different Na-ion full cells with Pb foil and other typical anodes. The details information for the cell components is given in supplementary materials. (d) The stack configurations for the energy density calculations.

Table II. The mechanical, electrical, and kinetical properties of Na-Pb phases.

Na-Pb phases	Elastic modulus (E)[49]	Bulk modulus (B)[49]	Shear modulus (G)[49]	B/G[49]	Electrical resistivity at 723 K/(Ohm·m)[50,51]	Na diffusivity in M or Na-M/(cm^2·s^{-1})
Pb	37.61	41.68	13.06	3.19	~1.00	~10^{-16} [37]
NaPb$_3$	28.23	32.94	3.90	3.90	~1.50	/
NaPb	24.72	15.04	1.50	1.50	~2.20	~5×10^{-17} [52]
Na$_9$Pb$_4$	N/A	N/A	N/A	N/A	~3.30	/
Na$_{15}$Pb$_4$	16.95	13.14	1.96	1.96	~4.00	~1×10^{-17} [52]

cycling stability of Pb electrodes since the XRD results suggest that a small amount of Na is trapped in the Na-Pb electrode that is desodiated to 0.8 V vs Na/Na$^+$ (#11 in Fig. 1b). While the Na trapping behaviors are rarely reported for Pb anode, rich literature can be found on the well-established Li-based chemistries where Li trapping is commonly ascribed to sluggish diffusion kinetics.[53] The diffusion-controlled Li trapping would give rise to the loss of active Li, thus leading to capacity degradation over cycling.[54] In the case of Pb electrodes, the trapped Na may also be associated with the different kinetic behaviors of different Na-Pb intermetallic phases. It should be noted that the kinetic limitations might be more pronounced in the metallic Pb foils than in their composite counterparts.[28]

The kinetic behaviors of the Na-Pb intermetallic phases remain poorly understood, with only three Na diffusivity values being calculated (Table II). The SEM images (Fig. 5) may be used to shed light on the Na diffusivity in Na-rich Na-Pb phases. Considerable voids are formed in the electrode (Fig. 5) after the desodiation when limited to the NaPb/Na$_9$Pb$_4$ transformations, in contrast to no obvious voids for the Na$_9$Pb$_4$/Na$_{15}$Pb$_4$ (Fig. S5d). Void formation is a well-known phenomenon in the interdiffusion process of metal alloy compounds since the dealloying strategy has been widely used to produce nanoporous alloy materials.[55] Meanwhile, many studies also reported the formation of pores in alloy electrodes in the desodiation or delithiation process, including Sn,[35] Al,[33] Si,[56] and Ge.[57] It is generally considered that the voids and/or pores formation

is a result of fast delithiation or desodiation kinetics.[56] The discussion seems contradictory to the theoretically calculated Na diffusivity of ~10^{-16} cm^2/s in Na$_{15}$Pb$_4$, which is around 1 order of magnitude slower than that in pristine Pb. In any case, systematic investigations using robust techniques or advanced instruments are needed to extract reliable Na diffusivities in these Na-Pb phases.

Strategic utilization of Pb foil anodes.—Given the poorest reversibility of NaPb/Na$_9$Pb$_4$, it is reasonable to strategically eliminate this problematic phase transformation by controlling the cutoff voltage from the electrochemical reactions of Pb anodes to prolong the cycle life and enable its utilization. This idea is further verified by the improved cycling performance of the Pb foil anode cycling within 0.15–0.8 V (Fig. S5) compared to the case of full sodiation-desodiation. To be specific, the Pb foil electrode delivers a reversible capacity of ~2.9 mAh·cm^{-2} after 20 cycles, corresponding to ~85% of the initial desodiation capacity.

The suitability of Pb foil as an SIB anode is evaluated by considering practical applications in terms of energy density. Figure 8a shows the Ragone plot of Na-ion cells with the Pb foil anode and other typical anodes (i.e., HC,[58–60] Sn,[14,59] Sb@TiO$_2$,[61] Sb@CNT,[62] and graphite[63]). The detailed parameters for the energy density calculation of the cells with NaMn$_{0.44}$O$_2$ cathode and 30 μm Pb foil anode (abbreviated as NMO//30Pb) are shown in Table S1. From Fig. 8a, one can see that the reported gravimetric energy data of the SIB cells ranges between 2–70 Wh·kg^{-1}, most of which are

higher than that of PABs (green zone, 30–40 Wh·kg^{-1} [64]), highlighting the competitiveness of SIBs over PABs in energy density. The NMO//30Pb cell stands between these reported results, delivering a gravimetric energy density of approximately 35 Wh·kg^{-1} (red star in Fig. 8a), slightly higher than PABs though lower than the present SIBs level (e.g., ~90–140 Wh·kg^{-1} (cell-level energy)[65]). This superiority of the Pb foil electrode in energy density is more pronounced when looking at the much higher volumetric energy density of the NMO//30Pb from Fig. S7, ~170 Wh·L^{-1}, than that of PABs. Notably, the NMO areal capacity is 0.9 mAh·cm^{-2}, much lower than the areal capacity requirement for the commercial battery (~2–3 mAh·cm^{-2} per side).[66] To better evaluate the future potential of Pb foil anodes, the typical O3 and P2 type cathodes with areal capacities of around 3 mAh·cm^{-2} are used for further energy density calculations. Figures 8b and 8c present the extrapolated gravimetric and volumetric energy density at stack level for different Na-ion cells with Pb foil anode and other typical anodes (i.e., HC, Sn/C, Sb/C, P/C, and Na$_2$Ti$_3$O$_7$ (NTO)). The simplified stack structures of the cells are shown in Fig. 8d and the detailed parameters of the cell components for the energy density calculation are given in Table S2.[67,68] While the cells with 30 μm-thick Pb foil anodes exhibit a higher gravimetric energy density than the one with NTO anodes, the value is found to be roughly 20%–30% lower than the cells with HC anodes or other alloy anodes (Fig. 8b). Intriguingly, the Pb foil anodes are more competitive in terms of volumetric energy density. As illustrated in Fig. 8c, the cells with Pb foil electrodes display the highest volumetric energy density (roughly 700 Wh·L^{-1}) among all the cells including those with Sn or Sb alloys anodes, which are regarded as the promising high-volumetric capacity anodes for SIBs. However, it is worth mentioning that the ratio of Pb foil (30 μm-thick) anode to cathode capacity is ~5.22, much higher than the normal level of N/P ratio (1.1–1.2) in commercial batteries.[69] For a better comparison, a 6 μm-thick Pb foil, which gives a more realistic N-to-P ratio (~1.09) is used to recalculate the energy density. By doing so, the superiority of the Pb foil anode becomes evident: Both the gravimetric (~180 Wh·kg^{-1}) and the volumetric energy density (850 Wh·L^{-1}) are the highest among all the cells presented in Figs. 8b and 8c. In this regard, Pb seems to be a feasible SIB electrode candidate and worth our further investigation, especially taking the low cost and abundance of Pb into account.

Summary

The Pb foil electrode exhibits an initial specific capacity of ~480 mAh·g^{-1} at 0.1 mA (12 mm electrode disk) but stops functioning after only 3–4 cycles. The XRD tests support the formation of the four Na-Pb intermetallic phases during sodiation, namely NaPb$_3$, NaPb, Na$_9$Pb$_4$, and Na$_{15}$Pb$_4$. It is found that some stubborn Pb regions are not sodiated even after the deep sodiation to 0.001 V vs Na/Na$^+$, while Na trapping is observed in the Na-Pb electrode after desodiating to 0.8 V vs Na/Na$^+$, perhaps due to the sluggish kinetics and/or complex microstructures. The SEM observations show that the electrode morphology changes dramatically during electrochemical cycling. The surface morphology of the Pb foil is found to be more catastrophically evolving with a higher Na content during the initial sodiation while Na extraction seems to result in the formation of cracks, voids, and mossy structures, largely explaining the fast capacity fading. To understand which phase transformations make a greater contribution to capacity fading, the reversibility of each pair of phase transformations is explored in isolation. Generally and reasonably, poorer reversibility of the phase transformations is expected at a higher sodiation depth (i.e., a higher volume change as compared to pristine Pb). Unexpectedly, we identified that the reversibility between NaPb and Na$_9$Pb$_4$ is noticeably poorer than that between Na$_9$Pb$_4$ and Na$_{15}$Pb$_4$, though both phase transformation pairs cause comparable volume changes. Not only can the poorest reversibility of the problematic phase transformations be well supported by the SEM analyses, but it is also well-aligned with the literature regarding the lattice volumes, mechanical properties,

electrical resistivity, and kinetic behaviors of these Na-Pb phases. Lastly, we proposed that the Pb electrode should be cycled within a narrower voltage range to largely exclude the problematic phase transformations. It is anticipated that this study can provide guidance for better utilization and development of Pb foil electrodes in SIBs.

ORCID

Tianye Zheng https://orcid.org/0000-0002-2281-9506
Steven T. Boles https://orcid.org/0000-0003-1422-5529

References

1. C. Vaalma, D. Buchholz, M. Weil, and S. Passerini, *Nat. Rev. Mater.*, **3**, 1 (2018).
2. H. Zhu, Z. Jia, Y. Chen, N. Weadock, J. Wan, O. Vaaland, X. Han, T. Li, and L. Hu, *Nano Lett.*, **13**, 3093 (2013).
3. Y. Li, Y. Lu, P. Adelhelm, M.-M. Titirici, and Y.-S. Hu, *Chem. Soc. Rev.*, **48**, 4655 (2019).
4. S. Wang, J. Fu, Y. Liu, R. S. Saravanan, J. Luo, S. Deng, T.-K. Sham, X. Sun, and Y. Mo, *Nat. Commun.*, **14**, 7615 (2023).
5. Y. Zhu, Z. Qian, J. Song, W. Du, J. Pan, D. Wang, and J. Yang, *Nano Lett.*, **21**, 3588 (2021).
6. X. Chen et al., *Adv. EnergyFunct. Mater.*, **12**, 2200886 (2022).
7. X. Chen et al., *Energy Environ. Sci.*, **16**, 4041 (2023).
8. M. Zhang, Y. Li, F. Wu, Y. Bai, and C. Wu, *Nano Energy*, **82**, 105738 (2021).
9. N. Sun, H. Liu, and B. Xu, *J. Mater. Chem. A*, **3**, 20560 (2015).
10. H. Tan, D. Chen, X. Rui, and Y. Yu, *Adv. Funct. Mater.*, **29**, 1808745 (2019).
11. J. Zhang, T. Zheng, K.-W. E. Cheng, K.-H. Lam, and S. T. Boles, *J. Electrochem. Soc.*, **170**, 100518 (2023).
12. C. Kim, H. Kim, M. K. Sadan, M. Jeon, G. Cho, J. Ahn, K. Kim, K. Cho, and H. Ahn, *Small*, **17**, 2102618 (2021).
13. C. Kim, I. Kim, H. Kim, M. K. Sadan, H. Yeo, G. Cho, J. Ahn, J. Ahn, and H. Ahn, *J. Mater. Chem. A*, **6**, 22809 (2018).
14. M. Song, C. Wang, D. Du, F. Li, and J. Chen, *Sci. China Chem.*, **62**, 616 (2019).
15. X. Lu, E. R. Adkins, Y. He, L. Zhong, L. Luo, S. X. Mao, C.-M. Wang, and B. A. Korgel, *Chem. Mater.*, **28**, 1236 (2016).
16. J. Ni, L. Li, and J. Lu, *ACS Energy Lett.*, **3**, 1137 (2018).
17. J. Sun, M. Li, J. A.-S. Oh, K. Zeng, and L. Lu, *Mater. Technol.*, **33**, 563 (2018).
18. S. Y. Sayed, W. P. Kalisvaart, E. J. Luber, B. C. Olsen, and J. M. Buriak, *ACS Appl. Energy Mater.*, **3**, 9950 (2020).
19. B. Farbod, K. Cui, W. P. Kalisvaart, M. Kupsta, B. Zahiri, A. Kohandehghan, E. M. Lotfabad, Z. Li, E. J. Luber, and D. Mitlin, *ACS Nano*, **8**, 4415 (2014).
20. Y. Fang, X. Yu, and X. Lou, *Angew. Chem. Int. Ed.*, **57**, 9859 (2018).
21. R. Amatya and R. Ram, *J. Electron. Mater.*, **41**, 1011 (2012).
22. J. Park, J. Han, J. Gim, J. Garcia, H. Iddir, S. Ahmed, G.-L. Xu, K. Amine, C. Johnson, and Y. Jung, *Chem. Mater.*, **35**, 4171 (2023).
23. A. Darwiche, R. Dugas, B. Fraisse, and L. Monconduit, *J. Power Sources*, **304**, 1 (2016).
24. J. Eaves-Rathert, K. Moyer-Vanderburgh, K. Wolfe, M. Zohair, and C. L. Pint, *Energy Stor. Mater.*, **35**, 552 (2022).
25. M. D.-L. Garayt, L. Zhang, Y. Zhang, M. C. Obialor, J. Deshmukh, Y. Xing, C. Yang, M. Metzger, and J. R. Dahn, *J. Electrochem. Soc.*, **171**, 070523 (2024).
26. C. Kim, H. Kim, M. K. Sadan, M. Jeon, C. Cho, T.-H. Nam, K.-K. Cho, J.-H. Ahn, and H.-J. Ahn, *J. Alloys Compd.*, **886**, 161240 (2021).
27. T. Jow, L. Shacklette, M. Maxfield, and D. Vernick, *J. Electrochem. Soc.*, **134**, 1730 (1987).
28. L. Ellis, B. Wilkes, T. Hatchard, and M. Obrovac, *J. Electrochem. Soc.*, **161**, A416 (2014).
29. S. Komaba, Y. Matsuura, T. Ishikawa, N. Yabuuchi, W. Murata, and S. Kuze, *Electrochem. Commun.*, **21**, 65 (2012).
30. T. Zheng and S. T. Boles, *ACS Omega*, **7**, 37867 (2022).
31. B. T. Heligman and A. Manthiram, *ACS Energy Lett.*, **6**, 2666 (2021).
32. C. Wang, Y. Meng, G. Ceder, and Y. Li, *J. Electrochem. Soc.*, **155**, A615 (2008).
33. T. Zheng, D. Kramer, M. H. Tahmasebi, R. Mönig, and S. T. Boles, *ChemSusChem*, **13**, 5910 (2020).
34. T. Li, U. Gulzar, X. Bai, M. Lenocini, M. Prato, K. E. Aifantis, C. Capiglia, and R. P. Zaccaria, *ACS Appl. Energy Mater.*, **2**, 860 (2019).

35. T. Li, U. Gulzar, R. Proietti Zaccaria, C. Capiglia, S. A. Hackney, and K. Aifantis, *J. Phys. Chem. C*, **123**, 15244 (2019).
36. S. C. DeCaluwe, B.-M. Dhar, L. Huang, Y. He, K. Yang, J. P. Owejan, Y. Zhao, A. A. Talin, J. Dura, and H. Wang, *Phys. Chem. Chem. Phys.*, **17**, 11301 (2015).
37. Y. Deng, J. Zheng, Q. Zhao, J. Yin, P. Biswal, Y. Hibi, S. Jin, and L. A. Archer, *Small*, **18**, 2203409 (2022).
38. K. Dong, H. Markotter, F. Sun, A. Hilger, N. Kardjilov, J. Banhart, and I. Manke, *ChemSusChem*, **12**, 261 (2019).
39. X. Yan, F. Ye, Y. Zhang, L. Lin, B. Sa, F. Liu, J. Li, L. Wang, J. Lin, and Q. Xie, *Chem. Eng. J.*, **440**, 135827 (2022).
40. B. Horstmann, J. Shi, R. Amine, M. Werres, X. He, H. Jia, F. Hausen, I. Cekic-Laskovic, S. Wiemers-Meyer, and J. Lopez, *Energy Environ. Sci.*, **14**, 5289 (2021).
41. S. W. Lee, M. T. McDowell, J. W. Choi, and Y. Cui, *Nano Lett.*, **11**, 3034 (2011).
42. T. Zheng, X. Wang, E. Jain, D. Kramer, R. Mönig, M. Seita, and S. T. Boles, *Scr. Mater.*, **188**, 164 (2020).
43. M. Pharr, K. Zhao, X. Wang, Z. Suo, and J. J. Vlassak, *Nano Lett.*, **12**, 5039 (2012).
44. Y.-S. Choi, J.-H. Park, J.-P. Ahn, and J.-C. Lee, *Chem. Mater.*, **31**, 1696 (2019).
45. G. Lamprecht, L. Dicks, and P. Crowther, *J. Phys. Chem.*, **72**, 1439 (1968).
46. L. Baggetto, P. Ganesh, R. P. Meisner, R. R. Unocic, J.-C. Jumas, C. A. Bridges, and G. M. Veith, *J. Power Sources*, **234**, 48 (2013).
47. V. A. Sethuraman, V. Srinivasan, A. F. Bower, and P. R. Guduru, *J. Electrochem. Soc.*, **157**, A1253 (2010).
48. D. A. Santos, J. L. Andrews, Y. Bai, P. Stein, Y. Luo, Y. Zhang, M. Pharr, B.-X. Xu, and S. Banerjee, *Mater. Horizons*, **7**, 3275 (2020).
49. M. Mortazavi, J. Deng, V. B. Shenoy, and N. V. Medhekar, *J. Power Sources*, **225**, 207 (2013).
50. C. V.-D. Marel, A. B.-V. Oosten, W. Gertsma, and W. V.-D. Lugt, *J. Phys. F: Met. Phys.*, **12**, 2349 (1982).
51. W. Calaway and M.-L. Saboungi, *J. Phys. F: Met. Phys.*, **13**, 1213 (1983).
52. Y. H. Kim et al., *Adv. Mater.*, **34**, e2201446 (2022).
53. P. J. Crowley, K. P. Scanlan, and A. Manthiram, *J. Power Sources*, **546**, 231973 (2022).
54. Y. Li, X. Zheng, Z. Cao, Y. Wang, Y. Wang, L. Lv, W. Huang, Y. Huang, and H. Zheng, *Energy Stor. Mater.*, **55**, 660 (2023).
55. J. Erlebacher, M. J. Aziz, A. Karma, N. Dimitrov, and K. Sieradzki, *Nature*, **410**, 450 (2001).
56. X. Lu, T. D. Bogart, M. Gu, C. Wang, and B. A. Korgel, *J. Phys. Chem. C*, **119**, 21889 (2015).
57. T. D. Bogart, X. Lu, M. Gu, C. Wang, and B. A. Korgel, *RSC Adv.*, **4**, 42022 (2014).
58. Y. Cao, Y. Liu, D. Zhao, X. Xia, L. Zhang, J. Zhang, H. Yang, and Y. Xia, *ACS Sustain. Chem. Eng.*, **8**, 1380 (2019).
59. A. Ponrouch, R. Dedryvère, D. Monti, A. E. Demet, J. M. Ateba Mba, L. Croguennec, C. Masquelier, P. Johansson, and M. R. Palacín, *Energy Environ. Sci.*, **6**, 2361 (2013).
60. L. Mu, S. Xu, Y. Li, Y. S. Hu, H. Li, L. Chen, and X. Huang, *Adv. Mater.*, **27**, 6928 (2015).
61. N. Wang, Z. Bai, Y. Qian, and J. Yang, *Adv. Mater.*, **28**, 4126 (2016).
62. J. Z. Guo, P. F. Wang, X. L. Wu, X. H. Zhang, Q. Yan, H. Chen, J. P. Zhang, and Y. G. Guo, *Adv. Mater.*, **29**, 1701968 (2017).
63. Z. L. Xu, G. Yoon, K.-Y. Park, H. Park, O. Tamwattana, S. Joo Kim, W. M. Seong, and K. Kang, *Nat. Commun.*, **10**, 2598 (2019).
64. Z. Cao and B. Wei, *Energy Environ. Sci.*, **6**, 3183 (2013).
65. A. Rudola, A. J. Rennie, R. Heap, S. S. Meysami, A. Lowbridge, F. Mazzali, R. Sayers, C. J. Wright, and J. Barker, *J. Mater. Chem. A*, **9**, 8279 (2021).
66. T. Zheng and S. T. Boles, *Prog. Energy*, **5**, 032001 (2023).
67. J. Zhang, T. Zheng, K.-H. Lam, and S. T. Boles, *Electrochim. Acta*, **456**, 142437 (2023).
68. I. Hasa, S. Mariyappan, D. Saurel, P. Adelhelm, A. Y. Koposov, C. Masquelier, L. Croguennec, and M. Casas-Cabanas, *J. Power Sources*, **482**, 228872 (2021).
69. H. Li, *Joule*, **3**, 911 (2019).